



**CHALMERS**  
UNIVERSITY OF TECHNOLOGY

## Mass Transport in “Water-in-Polymer Salt” Electrolytes

Downloaded from: <https://research.chalmers.se>, 2025-12-05 03:12 UTC

Citation for the original published paper (version of record):

Khan, Z., Martinelli, A., Rezende Franco, L. et al (2023). Mass Transport in “Water-in-Polymer Salt” Electrolytes. *Chemistry of Materials*, 35(16): 6382-6395.

<http://dx.doi.org/10.1021/acs.chemmater.3c01089>

N.B. When citing this work, cite the original published paper.

# Mass Transport in “Water-in-Polymer Salt” Electrolytes

Published as part of the Chemistry of Materials virtual special issue “In Honor of Prof. Elsa Reichmanis”.

Ziyauddin Khan,\* Anna Martinelli, Leandro R. Franco, Divyaratan Kumar, Alexander Idström, Lars Evenäs, C. Moyses Araujo, and Xavier Crispin\*



Cite This: *Chem. Mater.* 2023, 35, 6382–6395



Read Online

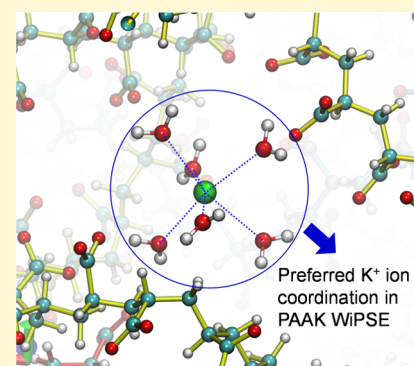
ACCESS |

Metrics & More

Article Recommendations

Supporting Information

**ABSTRACT:** “Water-in-polymer salt” electrolytes (WiPSEs) based on potassium polyacrylate (PAAK) belong to a new family of “water-in-salt” electrolytes that is envisioned as a potential solution for large-scale supercapacitors to balance the electric grid at short time scales. The WiPSEs display a broad electrochemical stability window up to 3 V, yet they are nonflammable and provide high ionic conductivity (100 mS/cm) as required in high-power devices. However, the transport of matter in PAAK-based WiPSEs has not been studied. In this work, we have extensively characterized PAAK by spectroscopic methods such as Raman spectroscopy and NMR diffusometry to determine the state of water and elucidate the mechanism of ionic transport as well as its interplay with water and polymer chain dynamics, which reveals that a significant proportion of the transport in WiPSEs is attributed to hydrated cations. The results are further supported by molecular dynamics (MD) simulations. Finally, the potential of WiPSEs based on PAAK is demonstrated in an activated carbon-based supercapacitor operating up to 2 V with reasonable self-discharge. This proof of concept shows promise for low-cost and large-scale supercapacitors.



## INTRODUCTION

In the complex task of balancing the electrical grid, there is a need for a set of energy storage technologies operating at different time scales, ranging from seconds to hours, days, and even months. Solutions for short time scales require large-scale and high-power devices such as supercapacitors. Most of the current research is focused on large-scale batteries but considerably less on large-scale supercapacitors, while they could complement each other. For instance, a challenge faced by large-scale vanadium redox flow batteries is their delivery of low current density,<sup>1</sup> making it beneficial to integrate them with a large-scale supercapacitor to enable the market application.<sup>2</sup>

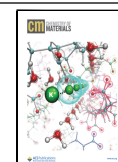
Large-scale supercapacitors require highly ionically conductive, nonflammable, and nontoxic electrolytes operable at high voltages, which can easily wet the low-cost electrodes such as activated carbons.<sup>3</sup> In commercialized secondary Li-ion batteries, organic electrolytes are typically utilized due to their stability within large working potential windows (3–4 V), thereby producing high specific energy ( $E = CV^2$ , where  $C$  is the specific capacity and  $V$  is the cell potential).<sup>4</sup> However, organic electrolytes suffer from low ionic conductivity, flammability, high cost, and environmental and sustainability issues. In contrast, water-based electrolytes are an attractive choice due to their high ionic conductivity, low cost, nonflammability, environmentally benign nature, sustainability, and high tolerance for moisture and oxygen, but they are limited by a narrow potential range of operation (1.2 V).<sup>5</sup>

One strategy that has been recently scrutinized is the use of water-in-salt electrolytes (WiSEs), since they provide the advantages of both aqueous electrolytes (high ionic conductivity and nonflammability) and organic electrolytes (high electrochemical stability windows, ESWs). These are superconcentrated electrolytes (typical concentration range being 4–10 M) with a mass, or volume, of salt that exceeds that of water.<sup>6</sup> A primary solvation sheath of water molecules around cations cannot form anymore and no water molecule remains free, i.e., having other water molecules as nearest neighbors. In 2015, Suo et al. prepared 5 M LiTFSI (lithium bis(trifluoromethane sulfonyl) imide) in water as a WiSE for Li-ion battery applications,<sup>6</sup> and later, the use of this type of electrolytes was extended to build high-voltage batteries, such as Na-, K-, and Zn-ion batteries.<sup>7</sup> The exceptional electrochemical stability of these superconcentrated aqueous electrolytes, far beyond 1.2 V, is impossible to achieve with conventional aqueous electrolytes. Numerous researchers endeavor to investigate the nature of water within highly concentrated electrolytic solutions, with the goal of expanding their ESWs and integrating them in high-voltage metal-ion

Received: May 9, 2023

Revised: July 14, 2023

Published: July 31, 2023



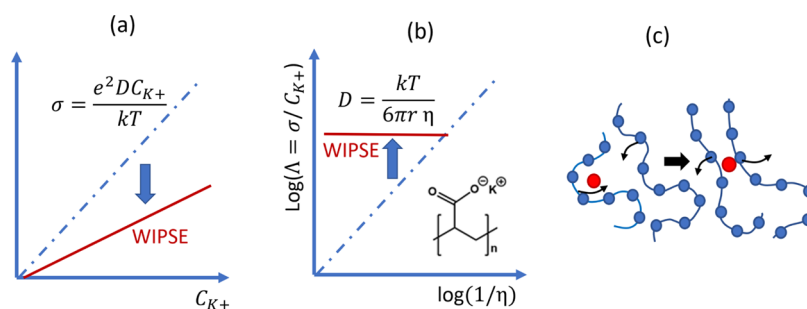


**Figure 1.** (a) Illustrating trend for the geometrical ionic conductivity  $\sigma$  versus ion concentration  $C_{K^+}$  for diluted K-salt solution (dashed line) and for the superconcentrated solution of PAAK (red line). (b) Effect of viscosity,  $\eta$ , on the molar conductivity,  $\Lambda$ . The diagonal represents the Angell reference line for diluted systems (dashed line), while the superconcentrated solution of PAAK displays a horizontal trend (red line). (c) Sketch of the dynamics of cation  $K^+$  hopping from one chain to the next chain driven by the local dynamics of the flexible polymer chains.

batteries.<sup>8</sup> Due to the high concentration of the electrolyte, the solvation structure of ions changes dramatically by disrupting the hydrogen-bond network; thus, resulting in a change in the electron cloud density of water molecules, which pushes the potentials associated with its redox processes beyond its normal limit.<sup>9</sup> Further, another mechanism identified to possibly contribute to the increase in ESW was the effect of local pH at the electrode/electrolyte interface and the water concentration.<sup>10</sup> The ion transport mechanism in WiSEs was investigated earlier using MD and small-angle neutron scattering.<sup>11,12</sup> In one of these studies, the authors demonstrated that increasing the concentration of LiTFSI from 10 to 21 m leads to the formation of a nanoheterogeneous liquid structure.<sup>11</sup> This phenomenon is caused by the coexistence of three types of ionic species: solvent-separated ion pairs (SSIPs), contact ion pairs (CIPs), and ionic aggregates (AGGs). The unusual nanoheterogeneity creates a three-dimensional (3D) percolating lithium–water network, which effectively releases cations from the anions' Coulombic traps. As a result, fast transport of  $Li^+$  cations is enabled at these high concentrations. Further, McEldrew et al. considered more complex and branched systems and developed a model to investigate the aggregation and gelation between cations, anions, and solvent molecules.<sup>13</sup> They concluded that high salt concentrations favor the formation of percolating gels, whereas low salt concentrations result in the presence of free ions only. In between these extremes, finite aggregates are formed. In several papers, WiSEs based on molecular salts seems to display a molar ionic conductivity ( $\Lambda$ ) that is inversely proportional to the macroscopic viscosity  $\eta$  (Figure 1b).<sup>14,15</sup> This trend is known as Walden's rule, which was derived for diluted solutions by using the Stokes–Einstein equation describing the ions as spheres with a hydrodynamic radius moving in a homogeneous fluid of viscosity.

One peculiar subclass of WiSEs has been proposed as “water-in-polymer salt” electrolytes (WiPSEs). Earlier studies report on the use of a highly concentrated metal cation polyacrylate (PAA) with either  $Li^+$  or  $K^+$ .<sup>16–18</sup> In particular, PAA $Li$  was fully integrated into a Li-ion battery operating at 2.6 V.<sup>16</sup> However, very little is understood about the transport of ions and water in WiPSEs. Polyacrylates are also known as superabsorbents<sup>19</sup> with very high solubility in water due to the flexibility of the polymer chains and their ability to create hydrogen bonds with water molecules. The WiPSEs based on PAAK display a high ionic conductivity ( $\sim 100$  mS/cm), proportional to the cation concentration (Figure 1a), and a large ESW ( $\sim 3$  V).<sup>15,17</sup> However, the conductivity is not fully

proportional to the cation concentration, which suggests that there is either a change in the self-diffusivity of ions with concentration or the formation of neutral aggregates or ion pairs that do not contribute to conductivity. An interesting observation was the constant molar ionic conductivity of water-in-PAAK electrolytes for various molecular weights of PAAK, despite viscosity varying by 4 orders of magnitude (Figure 1b).<sup>15</sup> This positioned WiPSEs within the class of superionic conductors according to the Angell reference line.<sup>20</sup> Such deviation of Walden's rule has been observed for “salt-in-polymer” electrolytes where the ion transport is driven by hopping activated by the microscopic dynamics of the polymer chains (Figure 1c).<sup>15</sup> It is, however, unknown if and how this mechanism takes place for a superconcentrated polymer electrolyte based on PAAK. Returning to the measurement of ESW, it is important to mention that water is limiting the ESW of the WiPSE, but it is not clear whether this is a thermodynamic or a kinetic effect. Hence, the characterization of the water and polymer diffusion in WiPSEs is highly relevant for further understanding the extraordinarily high ESW observed. To date, the mechanism of ionic transport as well as the dynamics of water and polymer diffusion in WiPSEs has never been investigated. The motivation of this work is to fill this gap of knowledge.

In this work, we have investigated the mass transport of ions, polymer chains, and water molecules in WiPSEs based on PAAK with experimental techniques such as Raman spectroscopy and pulsed-field gradient NMR spectroscopy. The presence of interacting water molecules and fully dissociated polyanions (PAA $^-$ ) and cations ( $K^+$ ) disrupt the H-bonded network of water. As expected, the self-diffusivity of both water and polymer increases as the concentration of WiPSEs decreases. Interestingly the activation energies for water diffusion (18.4 kJ/mol) and cation transport (18.5 kJ/mol) are similar, indicating an interplay for their transport, which was further analyzed by molecular dynamics simulations. Finally, the WiPSEs based on PAAK were integrated into supercapacitors to demonstrate their actual performance.

## RESULTS AND DISCUSSION

**Raman Spectroscopic Studies of WiPSEs.** PAAK-based electrolytes of different concentrations were prepared according to a previously reported procedure.<sup>15,17</sup> The four samples were chosen and labeled as PAAK 1:1, PAAK 1:2, PAAK 1:4, and PAAK 1:6, where the ratios represent the PAAK/ $H_2O$  weight ratio. Raman spectra were collected at room temperature for all four polymer electrolytes, as well as for pure water

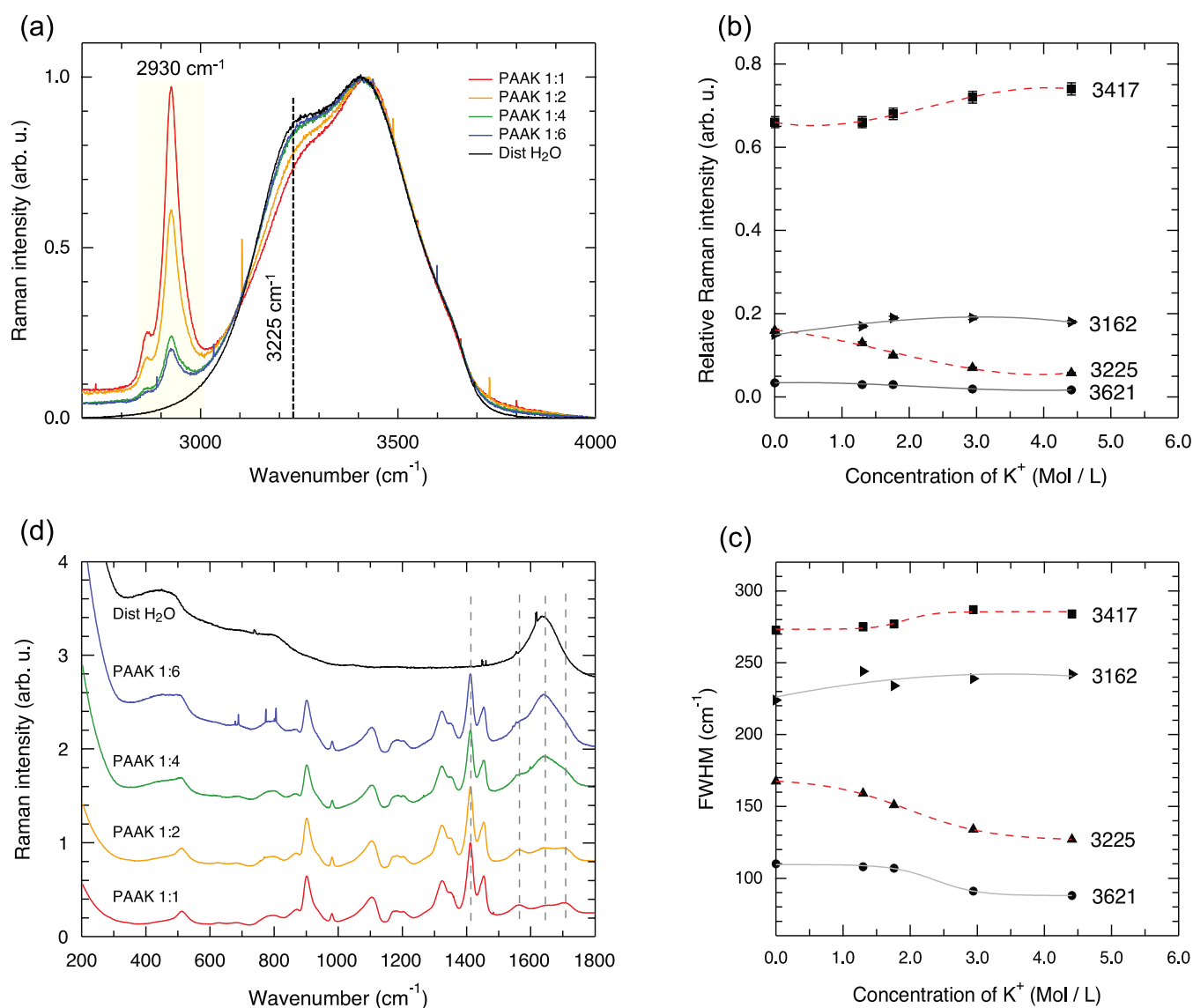


**Figure 2.** (a) Raman spectra of all four WIPSEs (colors) and distilled water (black) collected at room temperature. (b) Relationship between areas under the spectral profile obtained by fitting for different bands as a function of the concentration of  $\text{K}^+$  ions. (c) Width of the fitting peak as a function of composition. (d) Low-frequency region of the Raman spectra, where the polymer chain mainly contributes.

to compare. To accurately analyze the high-frequency spectral region, spectra were brought to zero at the highest frequency point and normalized to unity at  $\sim 3410 \text{ cm}^{-1}$ . After applying this normalization, some clear trends can be observed (Figure 2a). The feature at  $\sim 2930 \text{ cm}^{-1}$ , arising from the C–H stretching modes of the polymer, increases in intensity from sample PAAK 1:6 to sample PAAK 1:1, as expected due to the increased relative amount of PAAK in the sampled volume. Also, in the characteristic region of the O–H stretching modes of  $\text{H}_2\text{O}$  between  $3000$  and  $3800 \text{ cm}^{-1}$ , the lower frequency shoulder at  $\sim 3225 \text{ cm}^{-1}$  reveals a clear composition dependence, decreasing in intensity from PAAK 1:6 to PAAK 1:1.

For a better understanding of these changes, the Raman spectra were peak-fitted using a linear background and four Gaussian functions, according to the model that addresses the presence of hydrogen bonds and accounts for the configurations D–D, A–A, D–AA, etc. (D and A referring to donor and acceptor sites in a hydrogen bond, respectively). The obtained fit results are shown in Figure S4a–e in the Supporting Information (SI). The two main contributions

centered at  $3417$  and  $3225 \text{ cm}^{-1}$  can be ascribed to different types of hydrogen bondings and have been assigned to either stronger ( $3225 \text{ cm}^{-1}$ ) and weaker ( $3417 \text{ cm}^{-1}$ ) hydrogen bonds or to hydrogen bonds of types DDA/DAA ( $3225 \text{ cm}^{-1}$ ) and DD/AA ( $3417 \text{ cm}^{-1}$ ). Despite the different terminologies used, the two scenarios can be considered equivalent.

Further, the integrated area under the spectral profiles was also investigated, which is plotted in Figure 2b. The plot shows that with an increase in the concentration of  $\text{K}^+$  ions, the fraction of more weakly bound water molecules increases (the area under the peak at  $3417 \text{ cm}^{-1}$ ) and that of more strongly bound water molecules decreases (the area under the peak at  $3225 \text{ cm}^{-1}$ ), relative to the case of pure water. In other words, the decrease of the contribution at lower frequencies (at  $3225 \text{ cm}^{-1}$ ) with an increased polymer content reflects a lower fraction and/or degree of water–water hydrogen bonds. This is easily rationalized by the presence of  $\text{K}^+$  ions in the aqueous phase, which disrupts the intrinsic structure of water by interacting with the O atom that otherwise acts as hydrogen-bond acceptors. This type of structural change has previously

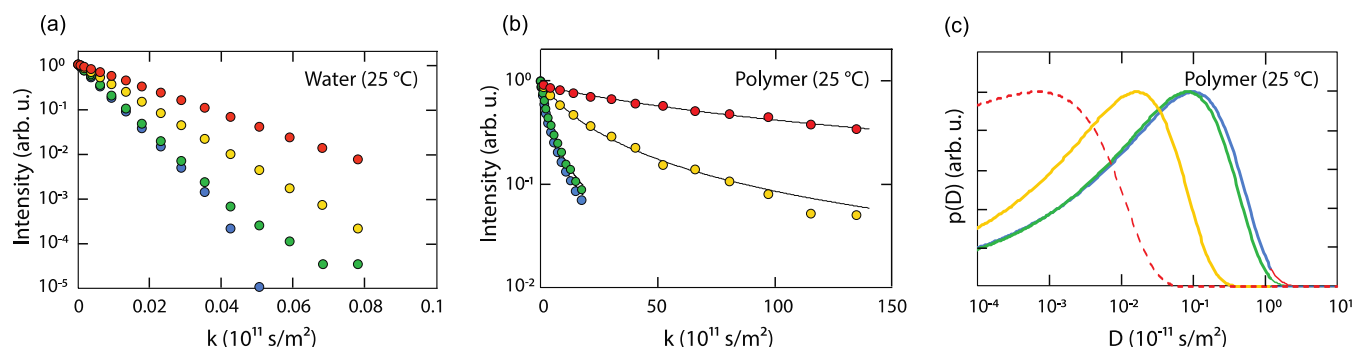


**Figure 3.** Attenuation of (a) H<sub>2</sub>O and (b) polymer signals for samples at 25 °C. The linear decay in (a) is associated with one single self-diffusion coefficient value. Solid lines in (b) represent the fitted  $\gamma$  distribution function for the attenuation of the polymer signal. (c) Distribution of polymer self-diffusion coefficients for all samples at 25 °C. The color code for the different samples is as in Figure 2, i.e., PAAK 1:6 in blue, 1:4 in green, 1:2 in yellow, and 1:1 in red.

been observed in classical electrolytes<sup>21</sup> and in neutralized PAA.<sup>22</sup> In the case of aqueous electrolytes, this induced structural change can affect the “local viscosity” and, in some circumstances, enhance the self-diffusion of water molecules compared to the case of pure water.<sup>21,23</sup> In our case, we believe that we are beyond the concentration range where these dynamic enhancements occur (i.e., above the concentration of 0.06 mol/L). In general, this structure-breaking effect has been observed in the Raman spectra of water upon the addition of different salts<sup>24</sup> and is equivalent to the effect of increasing the temperature as far as the weakening of hydrogen bonds is concerned. The evolution of the peak widths has also been investigated as a function of composition (Figure 2c). The full width at half-maximum (FWHM) of some peaks changes only marginally but that of the component at 3225 cm<sup>-1</sup> tends to narrow with an increasing amount of K<sup>+</sup> ions. More specifically, for the 3225 cm<sup>-1</sup> contribution at 4.4 M, we estimated a narrowing by 24% with respect to the case of pure water, which is comparable to the narrowing by ca. 20% in a 2 M solution of KBr.<sup>25</sup> A similar narrowing effect has previously been measured upon addition of salts like KBr, KI, and NaCl to water.<sup>26</sup> For both quantities, i.e., the relative Raman intensity and the FWHM of fitted peaks, it seems that a trend change occurs between the concentrations of 1.76 and 2.94 moles of K<sup>+</sup> per dm<sup>3</sup>, in other words, between samples PAAK 1:4 and PAAK 1:2.<sup>26</sup>

The low-frequency region of the Raman spectrum contains mainly vibrational modes arising from the polymer, along with the bending modes of water (Figure 2d). For comparison purposes, the spectra in Figure 2d have been normalized to the peak at 1412 cm<sup>-1</sup>, assigned to the COO<sup>-</sup> group of the polymer. The spectrum of PAAK 1:1, the less hydrated sample, is in perfect agreement with the Raman spectrum reported by Koda et al. for a fully neutralized PAA.<sup>27</sup> As explained by Koda et al.,  $I_{1413}/I_{1453}$  can be used as a probe of the degree of neutralization, since the band at 1413 cm<sup>-1</sup> is assigned to -COO<sup>-</sup>, while the band at 1453 cm<sup>-1</sup> is attributed to -CH<sub>2</sub>-bending of the backbone and is assumed to be insensitive to neutralization. From the Raman spectra shown in Figure 2d, we observe that the  $I_{1413}/I_{1453}$  ratio is a constant through composition (all of the other intensities below 1500 cm<sup>-1</sup> remain also unchanged), which suggests that the K<sup>+</sup> ions are dissociated from the polymer and are present in the aqueous phase in all of the electrolytes investigated.

Further, from PAAK 1:1 to PAAK 1:6, we observe an intensity increase of the mode at 1637 cm<sup>-1</sup>, assigned to the

O–H bending in water (fit peak 10 in Figure S5 in the SI), which is consistent with the increased relative amount of water in the electrolytes. The Raman spectra in this low-frequency region were also peak-fitted, with the assumption that additional information about the dissociation state of the -C=O group could be retrieved, as this region contains vibrational modes assigned to -C=O and -COO<sup>-</sup> and can provide more information about the location of the K<sup>+</sup> ions. However, the fit results could not be appropriately used, since the relevant signatures representing the polymer (at 1555, 1590, and 1622 cm<sup>-1</sup>) interfere too closely with the broad signature of water (O–H bending at 1637 cm<sup>-1</sup>), and quantitative estimations become difficult to achieve.

**Pulsed-Field NMR Spectroscopic Studies of WiPSEs.** A one-dimensional (1D) <sup>1</sup>H NMR spectrum recorded at 25 °C for sample PAAK 1:2 is shown in Figure S6 as a representative case, with the dominant water and hydroxyl signal to the left and the polymer hydrocarbon signals emphasized in the inset. In addition, to accurately determine the self-diffusion coefficients, the experimental parameters were adjusted to track the self-diffusion of water (high diffusivity) and the polymer (low diffusivity) in two subsequent measurements. For the case of water, a linear and monoexponential decay is observed in the familiar intensity versus  $k$  plot, indicating that only “one type” of water molecules is probed, Figure 3a, with respect to the self-diffusion coefficient. Hence, even though different types of water may be expected to coexist, these cannot be resolved during the experimental diffusion time (typically 100 ms) and only a population-average value is provided.

For the case of the polymer chain, the intensity versus  $k$  plots reveal a nonlinear trend, which reflects a distribution of diffusivity values (Figure 3b). This feature typically arises from the distribution of the molecular weight,  $M_w$ , but at this high concentration, additional effects may come from the presence of polymer entanglement that results in different local environments and consequently in a distribution of self-diffusion values. The distribution of the apparent polymer self-diffusion coefficients was obtained by fitting with the  $\gamma$  distribution function<sup>28</sup> shown as solid lines in Figure 3b. The calculated  $\gamma$  distribution is shown in Figure 3c and tends to broaden toward the low-value flank. This low-value broadening is most possibly due to the lack of experimental data for low signal intensities. From fitting with a  $\gamma$  function, a mean self-diffusion value is obtained for each sample. Moreover, sample PAAK 1:1 is shown as a dashed line to emphasize that greater

issues were encountered with this sample while trying to fit the collected data. Nonetheless, it should be remarked that the right side of the distribution, as well as the mean values, has high accuracy. The self-diffusion coefficients estimated by this approach, for water molecules and for the polymer phase, are summarized in Table 1; both increase systematically with the content of water.

**Table 1. Self-Diffusion Coefficients Calculated for the Temperature of 25 °C**

sample	$D_{\text{water}}$ ( $\times 10^{-11}$ m <sup>2</sup> /s)	$\langle D_{\text{polymer}} \rangle$ ( $\times 10^{-11}$ m <sup>2</sup> /s)	K <sup>+</sup> ion concentration (mol/L)	H <sub>2</sub> O/K <sup>+</sup> (mol/mol)
PAAK 1:1	63.7 ± 0.1	0.01	4.41	6
PAAK 1:2	107.7 ± 0.4	0.072 ± 0.005	2.94	12
PAAK 1:4	171.2 ± 0.7	0.37 ± 0.02	1.76	24
PAAK 1:6	182.4 ± 0.7	0.46 ± 0.02	1.3	36

In addition, the self-diffusion of water for sample PAAK 1:2 was also estimated as a function of temperature ranging from 10 to 50 °C, see Figure 4a. For all temperatures, a monoexponential, linear behavior is observed, and from the Arrhenius plot of diffusion values, an activation energy,  $E_a$ , of 18.4 kJ/mol could be obtained (Figure 4b). This can be compared to the value of 17.8 kJ/mol measured for pure water by Tanaka et al.<sup>29</sup> Herein, it is also shown that salts that decrease the self-diffusion of water are also those associated with higher activation energies for  $D_{\text{water}}$  (18.1 and 18.2 kJ/mol), which was explained by the fact that salts interacting strongly with water of hydration cause a translational slowdown. In that study, it was also shown that the addition of K-salts had a slight (or slightly positive) effect on  $D_{\text{water}}$ . Hence, we believe that the decrease of  $D_{\text{water}}$  observed with the increasing concentration of K<sup>+</sup> is, in the case of our WiPSEs, mainly an effect of physical obstructions caused by the polymeric chains and/or their entanglement, which can be explained by the effective medium theory.

Interestingly, we also measured the activation energy for ionic conduction by following the temperature-dependent ionic conductivity of PAAK 1:2 in the temperature range of 5–40 °C (Figure S7). The ionic conductivity changes linearly with inverse temperature (Figure 4c), and from the Arrhenius plot, an activation energy,  $E_a$ , of 18.5 kJ/mol could be

estimated. The value of activation energy for the K<sup>+</sup> cations and that for the H<sub>2</sub>O molecule (obtained by NMR) agree very well (Figure 4b). This congruence must mean that the K<sup>+</sup> ions (mainly responsible for the ionic conductivity reported in Figure 4c) are in the water phase, since the activation energy indicates the same diffusivity as water molecules (responsible for the data in Figure 4b).

The self-diffusion coefficients of water and the mean self-diffusion coefficients of the polymer are shown in Figure S8a, along with the values of the inverse of viscosity (measured macroscopically for the polymer electrolytes). It is observed that  $D_{\text{water}}$  and  $D_{\text{polymer}}$  decrease with different slopes, suggesting that they experience varying local viscosities. Also, trend-wise, the inverse of viscosity follows the behavior of the polymer better than that of water, which suggests that the macroscopically measured viscosity has a major contribution from the polymer phase and does not properly represent the local environment of the aqueous phase. To further convince that this is the case, we show in the plot of Figure S8c the experimentally determined  $D_{\text{water}}$  and  $D_{\text{water}}^*$  calculated using the Stokes–Einstein relation from viscosity and setting the radius of hydration for water equal to 1.05 Å, which ensures that  $D_{\text{water}}$  and  $D_{\text{water}}^*$  for pure water coincide in the absence of the polymer. Using the macroscopically measured viscosity,  $D_{\text{water}}^*$  falls well below the measured values, which cannot even be compensated by (realistically) adjusting the value of  $R_{\text{water}}$ .

The ionic conductivity of K<sup>+</sup> ions from the Nernst–Einstein relation using  $D_{\text{K}^+} = (R_{\text{water}}/R_{\text{K}^+}) \cdot D_{\text{water}}$  was estimated to compare with the experimental results and setting  $C$  equal to the concentration of K<sup>+</sup> in moles per dm<sup>3</sup> (i.e.,  $C$  is the molar concentration of ions). For clarity, the relation used for the estimated ionic conductivity is  $\sigma = (F^2/RT) \cdot D_{\text{K}^+} \cdot C$ , which includes the competing effects of decreasing  $D_{\text{K}^+}$  when  $C$  increases. The result of this analysis is shown in Figure S8b, where the measured conductivity is shown as light red symbols, while that estimated using the Nernst–Einstein relation is shown as dark red symbols. When we consider the simultaneous effect of an increasing number of charges together with the slowdown of the liquid phase in which these charges move, the trend experimentally measured is well reproduced by the equations.

Another interesting result is that for the polymer chain, the effect of temperature on diffusivity is different than that for water (which shows a linear trend in the Arrhenius plot, see Figure 4b). For all temperatures between 10 and 50 °C, a nonlinear behavior is observed; however, between 30 and 40 °C, a dramatic change is observed with an accompanying

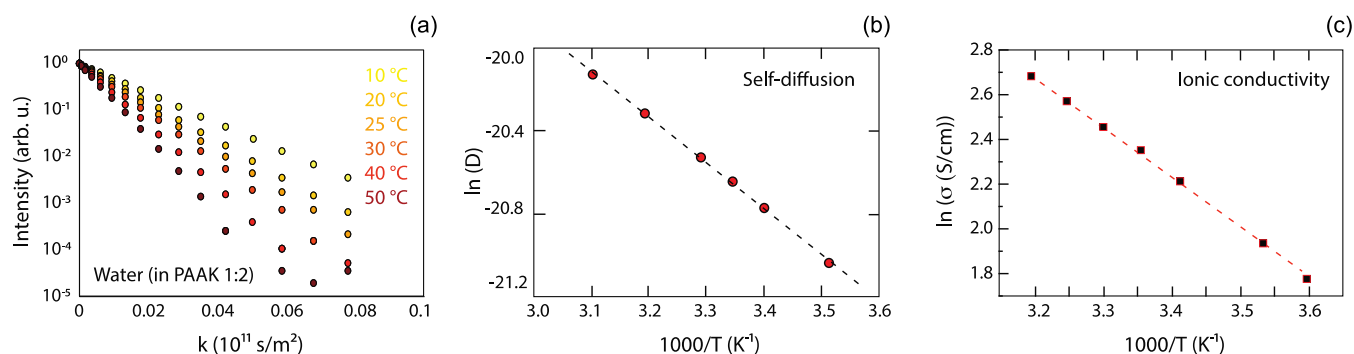


**Figure 4.** (a) Attenuation of the H<sub>2</sub>O signal for sample PAAK 1:2 at different temperatures, from 10 to 50 °C. (b, c) Arrhenius plots of  $D_{\text{water}}$  obtained from NMR studies and the ionic conductivity experimentally measured, respectively.

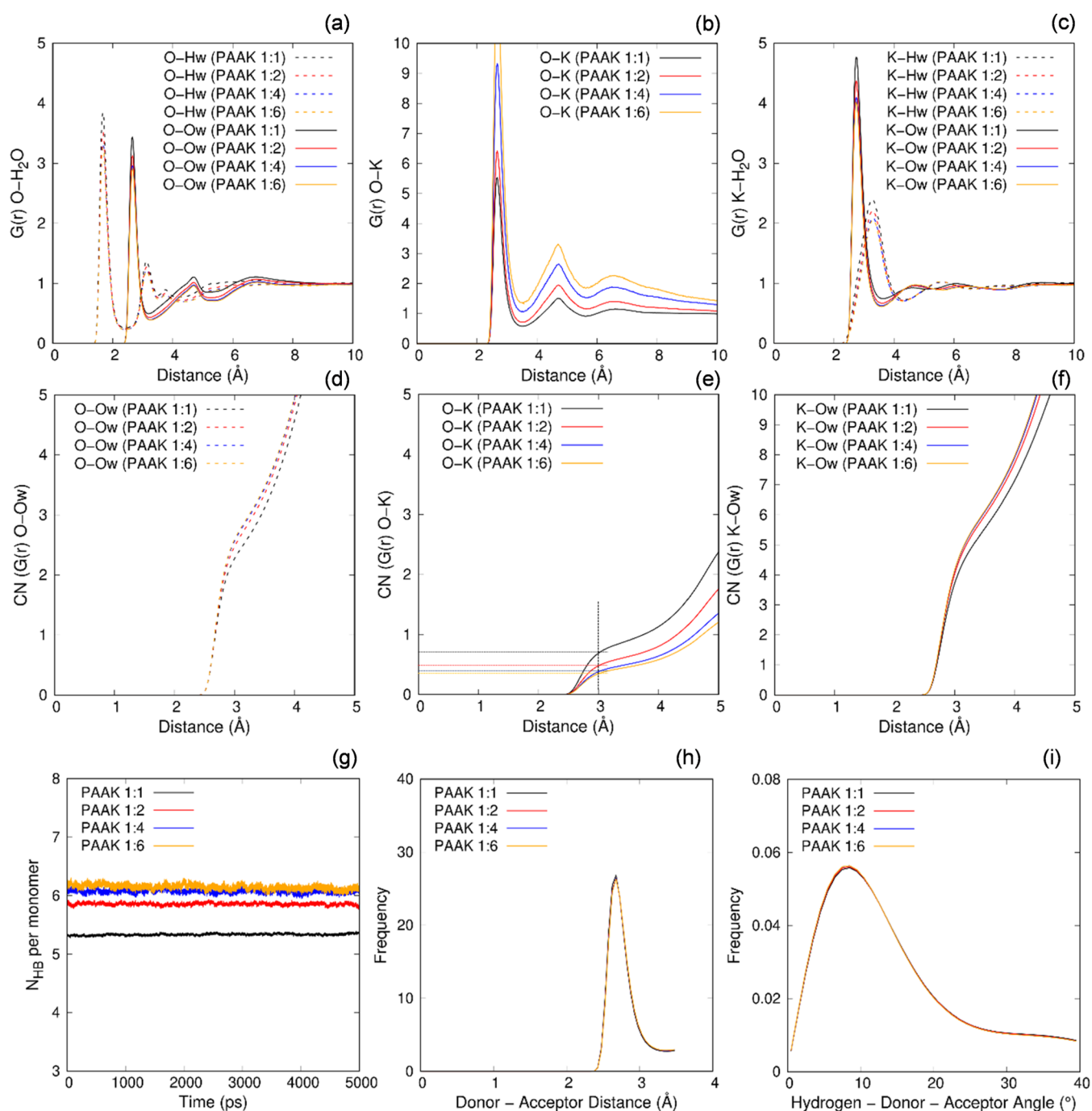


**Figure 5.** Panels (a)–(c) display the pair radial distribution functions,  $G(r)$ , for O with respect to  $K^+$ , Ow, and Hw. Panels (d)–(f) show the coordination numbers, CNs, which represent the number of particles surrounding each polymer oxygen, potassium ion, or water molecule. Panel (g) presents the number of hydrogen bonds per monomer ( $N_{HB}$ ). Panels (h) and (i) display the donor–acceptor distance and H–donor–acceptor angle distributions, respectively, for the hydrogen bonds between the polymer and water molecules.

significant shift and narrowing of the distribution curve (Figure S9). A clearer visualization of this temperature-induced change in diffusivity can be seen in the Arrhenius plot shown in Figure S10. Here, the first five data points of the signal attenuation were fitted with the monoexponential function as used for water to get a single self-diffusion coefficient. It should be noted that this calculated value is consistently  $0.79 \pm 0.04$  lower than the mean value for the distributions provided in Figures 3c and S9. The Arrhenius linearity is apparent from 10 °C up to 30 °C. Above 30 °C, that is, between 30 and 50 °C, a different slope is measured, indicating higher activation energy.

This may be due to a conformational change in the polymer, although we do not have further experimental evidence confirming this hypothesis.

**Theoretical Studies of the Polymer Salt Electrolyte in Aqueous Solution.** Classical molecular dynamics (MD) simulations for all PAAK samples were carried out at room temperature and pressure conditions ( $T = 298.15$  K,  $p = 1$  atm). The simulated systems, as illustrated in Figure S2, were composed of 43,000 water molecules and  $N$  ( $= 140$  for 1:1,  $= 70$  for 1:2,  $= 35$  for 1:4, and  $= 24$  for 1:6) PAA<sup>−</sup> polymers (with 50 monomers each) and  $50 \times N$   $K^+$  ions. Methodology

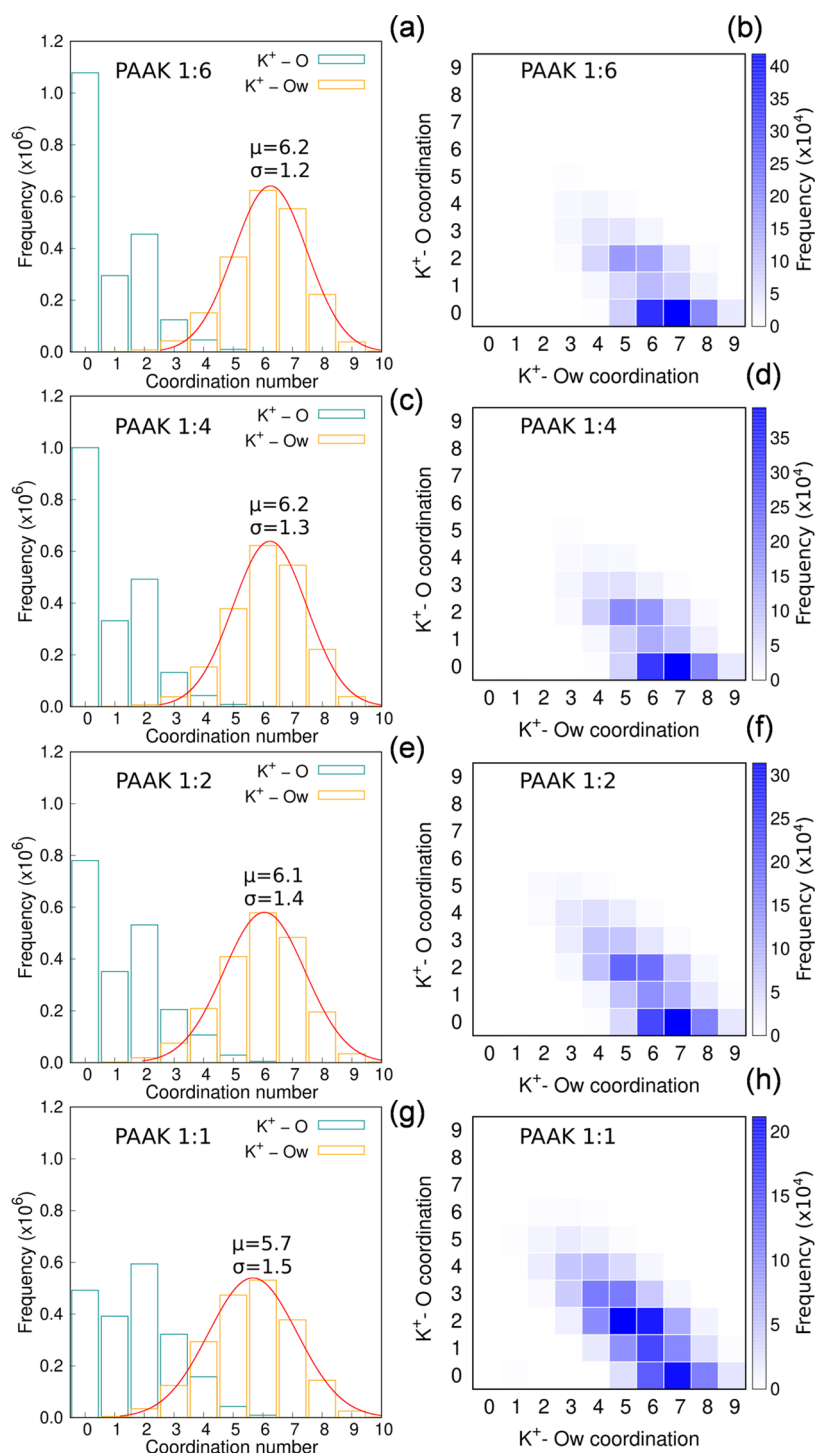


**Figure 6.** Coordination distribution of  $K^+$  by O and Ow at PAAK concentrations of (a) 1:6, (c) 1:4, (e) 1:2, and (g) 1:1. Relative contribution to the potassium total coordination with O and Ow at PAAK concentrations of (b) 1:6, (d) 1:4, (f) 1:2, and (h) 1:1.

details about these simulations are available in the SI. Figure 5a–c displays the pair radial distribution functions ( $G(r)$ ) between polymer oxygens (O), oxygen (Ow) and hydrogen (Hw) of water molecules, and potassium ions ( $K^+$ ). The well-defined peaks and valleys at shorter radial distances reveal at first that the microsolvation region around the polymers has a preferential structure. The first peak in  $G(r)^{O-Hw}$  ( $r = 0.17$  nm) shows that the atomic types found at the first vicinity of the polymer oxygens are the hydrogens of water molecules (Figure 5a). Furthermore, the  $G(r)^{O-K}$  and  $G(r)^{O-Ow}$  curves

have the first peak at the same radial distance of  $r = 0.27$  nm (Figure 5a,b), showing that there is a spatial competition between the  $K^+$  ions and water molecules to coordinate with the oxygen of the polymer. The differences in the intensities of the  $G(r)$  functions for different concentrations of the polymer electrolyte is a simple consequence of the average density of the simulation box, without any further impact on the structural analysis. Indeed, the minimum and maximum positions of the pair radial distributions functions do not depend on the polymer concentration, but their integrals show

that increasing the concentration of PAAK increases the potassium density in the polymer microsolvation regions (Figure 5e), which also contributes to a slight reduction in the coordination number between K and Ow in the long range (Figure 5f). At a radial distance of 0.30 nm from the O, the average numbers of interacting potassium ions are 0.71, 0.52, 0.43, and 0.35 at the 1:1, 1:2, 1:4, and 1:6 concentrations of PAAK (Figure 5e), respectively, which shows a decrease in the number of coordinated  $K^+$  ions compared to the polymer in vacuum. In vacuum, each monomer can coordinate to a maximum of two ions within a radial distance of 0.27 nm, as predicted by the DFT geometry optimization (see Figure S3). The number of hydrogen bonds ( $N_{HB}$ ) per monomer was also estimated, which decreases as the number of  $K^+$  ions near the polymer chain increases (Figure 5g). The estimated average  $N_{HB}$  per monomer are 6.2, 6.1, 5.8, and 5.3 for concentrations of 1:6, 1:4, 1:2, and 1:1, respectively, which occurs at a donor–acceptor distance of 0.27 nm and at a preferable hydrogen–donor–acceptor angle of  $8.5^\circ$  (see Figure 5h,i).

Despite the slight increase in the coordination number between the oxygen atoms of the polymer and  $K^+$  ions at higher polymer concentrations, the majority of  $K^+$  ions are primarily located within the water domains. The left panels of Figure 6 provide a detailed analysis of the microsolvation shell composition surrounding  $K^+$  in the simulated systems. Notably, the coordination distribution of  $K^+$  with Ow exhibits the highest coordination numbers, forming a Gaussian-shaped curve. The average coordination ( $\mu$ ) and half-width ( $\sigma$ ) values for the PAAK/ $H_2O$  weight ratios of 1:6, 1:4, 1:2, and 1:1 are  $\mu = 6.2$  and  $\sigma = 1.2$ ,  $\mu = 6.2$  and  $\sigma = 1.3$ ,  $\mu = 6.1$  and  $\sigma = 1.4$ , and  $\mu = 5.7$  and  $\sigma = 1.5$ , respectively. An observed trend is the consistent increase in the Gaussian width with the increase in salt concentration, which is connected to the interaction between  $K^+$  and polyanions. In contrast, the coordination distribution of  $K^+$  ions with O results in lower coordination numbers and lacks a clearly defined Gaussian shape. To further investigate the coordination patterns, the right panels of Figure 6 show the relative coordination matrix of  $K^+$  by different oxygens (from water or polyanions) throughout the MD trajectories. At lower polymer concentrations (1:6), the most frequently observed case is the coordination of  $K^+$  ions with 7 and 6 Ow and 0 O. As the polymer concentration increases, the probability of  $K^+$  ions coordinating with 6 and 7 Ow remains high, but mixed coordination becomes more common. In these cases, the probability of coordination between  $K^+$  ions and, for instance, 5 and 4 Ow, as well as 3 and 2 O, increases. Coordination with O is mapped as a rare event, even at the highest polymer concentration (PAAK 1:1). Figure S11a–c displays three frames of the PAAK 1:1 MD simulation, illustrating different microsolvation compositions of a  $K^+$  ion with only O, only Ow, and both in similar proportions, respectively.

The self-diffusion coefficients of water ( $D_{water}$ ), polymer ( $D_{polymer}$ ), and  $K^+$  ions ( $D_{K^+}$ ) were also evaluated from the linear slope of the molecular mean squared displacements (MSDs) over the MD trajectories, using the Einstein relation.<sup>30</sup> Figure S12 displays the calculated MSD for water, polymer, and  $K^+$ ; Table 2 presents the obtained values for the self-diffusion coefficients, for the different simulated PAAK concentrations. The MD results yield excellent agreement with the experimental data available in the literature for the self-diffusion coefficients of potassium ions and water molecules in pure water. Moreover, the simulations confirm the diffusion

**Table 2. Values of  $D_{water}$ ,  $D_{polymer}$ , and  $D_{K^+}$  ( $\times 10^{-11}$  m<sup>2</sup>/s) Obtained from MD Simulations for Solutions with Different Concentrations of PAAK at 298.15 K<sup>a</sup>**

sample	$D_{water}$	$D_{polymer}$ [ $D_{polymer}$ ]*	$D_{K^+}$
PAAK 1:1	$29.2 \pm 1.7$	$0.8 \pm 0.3$ [ $0.2 \pm 0.05$ ]	$11.6 \pm 0.6$
PAAK 1:2	$93.9 \pm 2.5$	$2.3 \pm 1.2$ [ $0.9 \pm 0.2$ ]	$41.3 \pm 0.1$
PAAK 1:4	$164.8 \pm 1.8$	$6.3 \pm 2.3$ [ $1.6 \pm 0.6$ ]	$70.4 \pm 1.0$
PAAK 1:6	$195.1 \pm 0.8$	$8.5 \pm 3.0$ [ $2.04 \pm 0.4$ ]	$86.6 \pm 1.9$

<sup>a</sup>Calculated  $D_{K^+}$  (in pure water)  $201.9 \pm 5.0$  (from the literature  $D_{K^+} = 196.0$ );<sup>31</sup> Calculated  $D_{water}$  (in pure water)  $258.3 \pm 0.9$  (from the literature  $D_{water} = 229.9$ );<sup>32</sup> [ $D_{polymer}$ ] values obtained from the average MSD of the atoms in the polymer chains; [ $D_{polymer}$ ]\* values obtained from the average MSD of the center of mass of polymer chains

trends of water, polymer, and potassium ions observed in both WiPSEs, across a concentration range of 4.4–1.3 M, and NMR studies (as detailed in Table 1). The self-diffusion coefficients of the polymer chains, calculated using atomic or center of mass MSD fitting, consistently exceed the experimental values. We attribute this discrepancy to the smaller size of our simulated polymer chains, which comprise only 50 monomers. Collectively, both experimental techniques and MD simulations reveal that reducing the concentration of PAAK leads to increased  $D_{water}$ ,  $D_{polymer}$ , and  $D_{K^+}$  values.

Besides the average sample analysis, we have investigated the effects of microsolvation composition on cation mobility. Specifically, we have focused on the relative coordination matrix of  $K^+$  and identified three distinct regions within the matrix (Figure 7a) to represent various scenarios of microsolvation for  $K^+$  ions. These scenarios include predominantly Ow (black cells), O (pink cells), and a combination of both (green cells) in similar proportions. We have examined the trajectories of  $K^+$  ions within each group over a time window of 1 ns. Our findings reveal that not only does the concentration of polymers impact cation mobility, but the composition of microsolvation also plays a significant role. At a concentration of PAAK 1:6, for example,  $K^+$  ions close to the O domain exhibit a self-diffusion coefficient approximately 4 times lower than that for those within the water domain. Remarkably, even a small number of three or four Ow coordinating with  $K^+$  is sufficient to induce a drastic change in its mobility within a mixed polymer/water domain. The variations observed in the cation mobility could be attributed to alterations in the dynamic interactions occurring within the cation microsolvation region. More specifically, the residence time analysis of  $K^+$  ions and their interactions with O and Ow (Figure 7b,c) demonstrates the connection between enhanced cation mobility and a decrease in the duration of interactions with O or Ow. The dynamic nature of these interactions plays a crucial role in governing cation mobility, as shorter interaction durations enable the cations to navigate through the solvation environment more freely.

Furthermore, the NMR results discussed above show that  $D_{water}$  increases three times, whereas  $D_{polymer}$  increases 46 times upon reducing the concentration of  $K^+$  ion from 4.4 to 1.3 M. Figure 8a presents the plot of measured  $D_{water}$  with water content (in %) for different PAAK electrolytes. This displays a remarkable linear dependency of  $D_{water}$  with water content. As the concentration of the electrolyte decreases, i.e., an increase in water content, the self-diffusion coefficient of water increases toward the value of bulk water. This kind of behavior

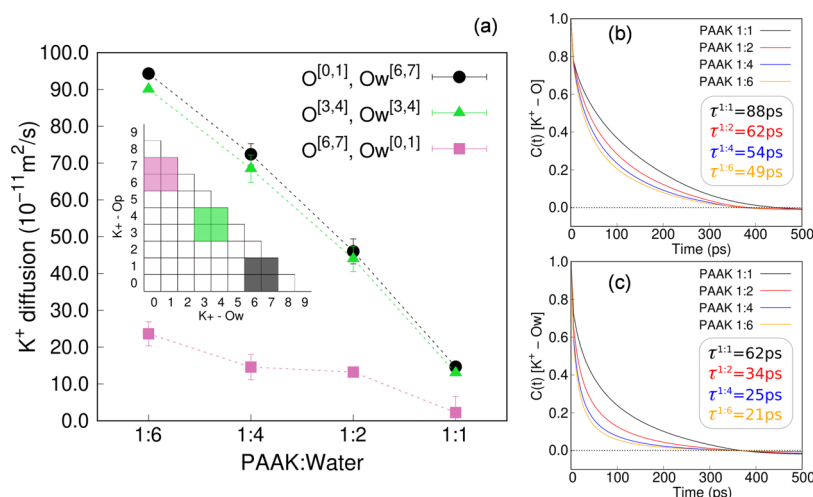


**Figure 7.** (a) Diffusion coefficients of  $K^+$  for different microsolvation environments under varying PAAK concentrations. The potassium ions were classified into three microsolvation groups: (pink color) maximized coordination with O, (black color) maximized coordination with  $O_w$ , and (green color) predominant coordination with both O and  $O_w$  in similar proportions. (b, c) Residence time ( $\tau$ ) of the  $K^+$ /oxygen (O or  $O_w$ ) coordination for varying PAAK concentrations.

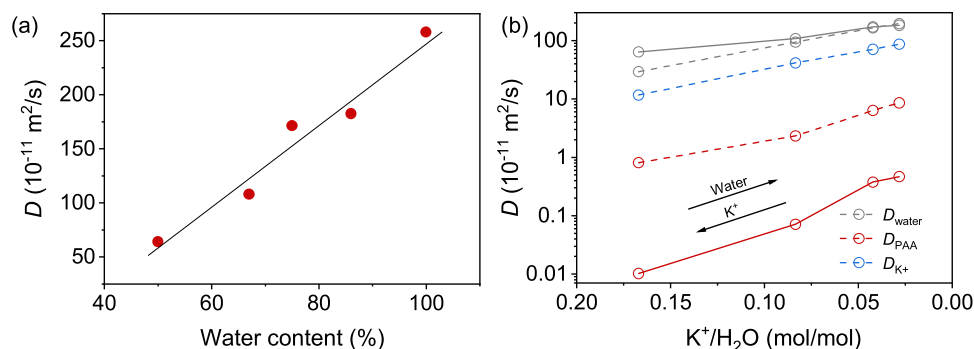


**Figure 8.** (a)  $D_{\text{water}}$  versus water content (%) plot illustrating that water content is the predominant factor in determining the  $D_{\text{water}}$  of WiPSEs. Pure water value was taken as 258.3, as presented in Table 2, whereas other data points for PAAK samples were taken from Table 1. (b) Diffusion coefficient of all components (water, polymer, and cations) of WiPSEs versus water content (%). The diffusion of all components increases with content, which can be explained by EMT. Dotted line data are from theoretical studies, and solid line presents data from our NMR studies.

is typically observed in hydrogels and water–sugar solutions.<sup>33</sup> Figure 8b shows the dependence of the self-diffusion coefficients of water, polymer, and  $K^+$  ions on the water content (%). The decrease in self-diffusion of water with an increase in the concentration of electrolytes could be explained using the effective medium theory (EMT) models in electrolytes. EMT models have been used to explain the dependence of the conductivities of composite polymeric electrolytes on the concentration of the filler added.<sup>34</sup> We believe that in high-concentration polymer electrolytes, the self-diffusion of water molecules is hindered by polymer chains, hence leading to a decreased  $D_{\text{water}}$  value with the concentration in the electrolytes.

Based on all findings, we can conclude the following: (i) The  $K^+$  ions are in the aqueous phase and the polymer is in the PAA<sup>-</sup> form (entirely dissociated) without the sign of any ion pair formation. (ii) The  $K^+$  ions induce a structural change in water by disrupting the H-bonded network (decrease of the  $3225 \text{ cm}^{-1}$  mode and  $N_{\text{HB}}$  decreases with high  $C_{K^+}$ ), which is expected for this cation, suggesting that free water reduces with an increase in ion concentration. (iii) Based on the actual concentration of  $K^+$  in the water phase ( $>1 \text{ mol/L}$ ) and on previous studies of salt electrolytes, the presence of  $K^+$  ions

should have a positive or negligible effect on  $D_{\text{water}}$ . The observed decrease in  $D_{\text{water}}$  with  $C_{K^+}$  is thus mainly an effect of physical obstruction (polymer chains). (iv) Moreover, the estimated value of  $E_a$  for  $D_{\text{water}}$  of 18.4 kJ/mol matching well with  $E_a$  for the ionic conductivity  $\sigma$  (i.e., 18.5 kJ/mol) suggests that the  $K^+$  ions and water diffuse together and perhaps that  $K^+$  ions move with the solvation shell through the electrolyte similar to the previous studies, revealing that transport in WiSEs comes from hydrated cations. Finally, we also observe a transition temperature of around  $30 \text{ }^\circ\text{C}$  for the polymer that, to the best of our knowledge, may be associated with a conformational change. Importantly, the results from MD simulations agree very well with experimental results, particularly in terms of the number of hydrogen bonds formed between the polymer and water as a function of electrolyte concentration.

**Application of PAAK for Electrochemical Energy Storage.** To verify the application of this type of electrolytes, the WiPSEs were tested in a real device where symmetric supercapacitors were built using activated carbon (AC) electrodes. The devices were built using different PAAK samples, which were tested using the galvanostatic charge–discharge method, increasing the potential of the device from 1

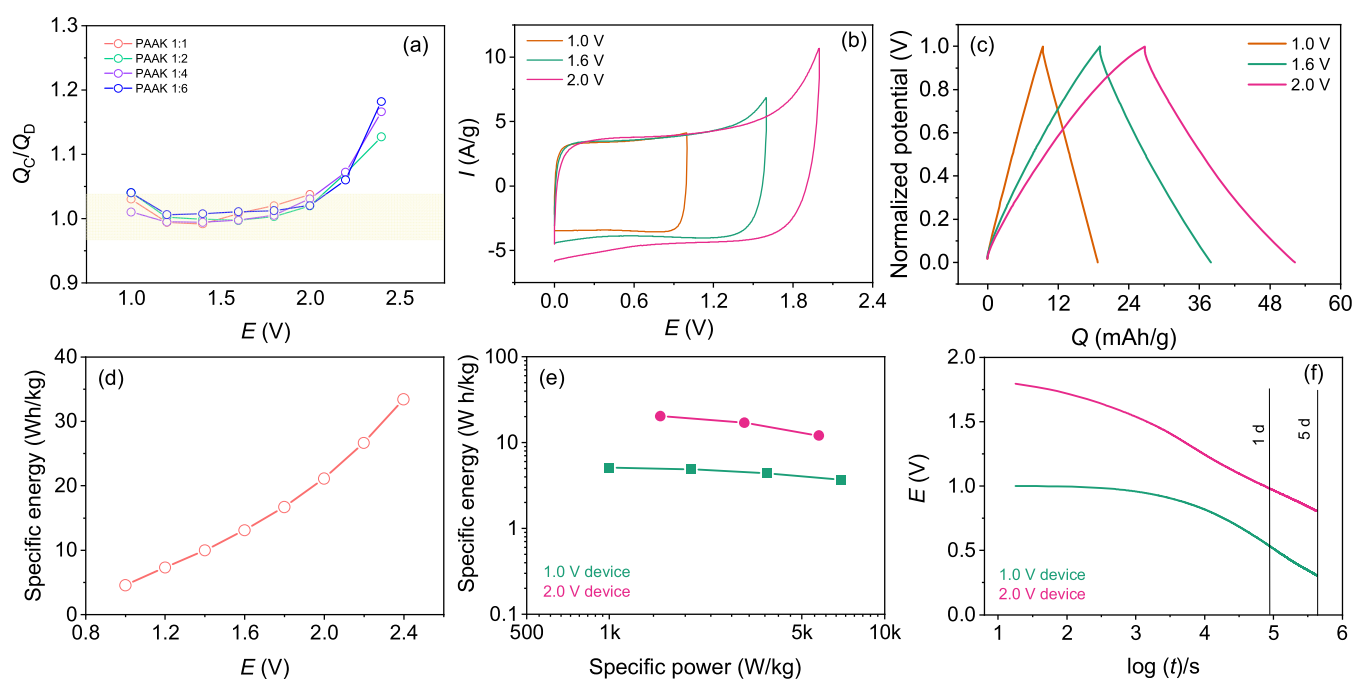


**Figure 9.** (a) Ratio of the integrated charges  $Q_C/Q_D$  for the charge curve and discharge curve with PAAK. (b) CV curves for the supercapacitor based on the AC electrode with PAAK 1:2 at a scan rate of 100 mV/s. (c) Galvanostatic charge–discharge characteristics at 4 A/g for different maximum voltages (1, 1.6, and 2.0 V) that are normalized to make an easy comparison. (d) Specific energy versus voltage obtained from the discharge curve at 4 A/g. (e) Ragone plot for PAAK at different current rates ranging from 2 to 16 A/g. (f) Self-discharge curve for PAAK charged at 1 and 2 V.

to 2.4 V. Therefore, the stable operable potential range could be estimated (please see the [Experimental Section](#) for more details on the testing method). The charging of the device leads to the formation of electric double layers at the large interfacial area between the carbon electrode and the electrolyte. The total charge for charge–discharge processes was quantified as the ratio  $Q_C/Q_D$  between the integrated charge during charge  $Q_C$  and discharge  $Q_D$  (Figure 9a). For a device with no or low leakage current associated with the redox process of water,  $Q_C/Q_D = \sim 1$ , whereas if the electrolyte undergoes a water electrolysis process, the number of charges required to achieve the charging potential of the device would be high; thus,  $Q_C/Q_D > 1$ . It is evident from Figure 9a that the ratio of  $Q_C$  and  $Q_D$  remains close to 1 for all of the devices up to 2 V. This ratio gradually increases with a further increase in potential up to 2.4 V and reaches 1.2 for the device with PAAK 1:6 WiPSE. It would be worth mentioning that beyond 2.4 V, all of the devices were not operable, probably due to cell shortening. Therefore, based on these results, the best operable voltage is 2 V due to the low leakage current generated through water electrolysis.

The supercapacitor device in PAAK 1:2 was further analyzed to estimate specific energy and self-discharge as a function of voltage. The PAAK 1:2 electrolyte was chosen to study the device further as it has a good  $Q_C/Q_D$  ratio, good ionic conductivity, and low viscosity (see [Table S1](#)) compared to PAAK 1:1, which makes it more user-friendly. The cyclic voltammograms (CVs) recorded for the increasing voltage range from 1 to 2 V (Figure 9b) display a rectangle shape with a tail at higher potentials. Charge–discharge characteristics are also recorded for increasing voltage ranges (same as in the CVs), and then these ranges are normalized in order to compare the shape of the curves (Figure 9c), while the charge–discharge curves for different potential ranges ([0–1],

[0–1.6 V], and [0–2]) are symmetric and quasi-symmetric for PAAK. The leakage current that was visible in the CVs at high voltages impacts the normalized charge–discharge curves (Figure 9c) by creating a small plateau at high voltages in the charge curve, which is absent in the discharge curve. This asymmetry between charge and discharge curves is visible when the cutoff charging potential was 2.0 V. The specific energy of the device was found to increase from 4.5 to 33.4 Wh/kg with voltage (Figure 9d). From the Ragone plot shown in Figure 9e, for a 2 V supercapacitor device, a maximum specific energy of 20 Wh/kg and a maximum power of 5.8 kW/kg can be achieved (corresponding CV and GCD plot has been provided in [Figure S13](#) in the SI).

Finally, the self-discharge is recorded starting from two different potentials (1 and 2 V) and plotted in Figure 9f. Regarding the mechanism of self-discharge in the AC/PAAK/AC supercapacitor, there is a correlation between the leakage current (deviation from  $Q_C/Q_D = 1$  in Figure 9c) increasing above 1 V and the shape of the self-discharge in Figure 9f that displays a fast rate in the high potential region until it reaches about 1 V. At 1 V, the rate of self-discharge at early time is constant and the leakage is negligible with  $Q_C/Q_D = 1$ . Hence, this suggests that the current associated with water electrolysis is the origin of the leakage current in the device as well as the major origin of the self-discharge mechanism. Importantly, compared to all other supercapacitors based on carbon electrodes and aqueous electrolytes found in the literature (some are reported in [Figure S14](#)), the AC/PAAK/AC supercapacitor possesses the best self-discharge behavior. This constitutes a breakthrough in the field of aqueous electrical energy storage combining safe and scalable attributes.

## CONCLUSIONS

The research for the application of “water-in-salt” electrolytes, so-called WISEs, in electrochemical energy storage devices has been growing tremendously, primarily utilizing the enlargement of the electrochemical stability window for the fabrication of high-energy batteries. WiPSEs, or “water-in-polymer salt” electrolytes, are a new class of WISEs that showed promise as a cost-effective nonflammable electrolyte solution for large-scale stationary energy storage devices to support grids. However, very little is known about the transport mechanism in these electrolytes, which is key to their performance. Herein, we characterized and elucidated the state of water in polymer electrolytes and the mechanism of ionic transport using Raman spectroscopy, diffusometry NMR, and MD simulations. Raman spectroscopy discloses that both polyanions and cations are in a fully dissociated state without forming any ion pair, and with an increase in the concentration of  $K^+$  ions, the disruption in the H-bond of water was also observed. The self-diffusion of water and the polymer determined by NMR reveals that both water and polymer diffusion is enhanced with a decrease in the concentration of the electrolyte. These two results were well supported by MD simulations. Interestingly, the activation energy for ionic migration ( $\sim 18$  kJ/mol) is close to the activation energy for  $H_2O$  diffusion, thus suggesting that  $K^+$  ions migrate in the water phase rather than following the local dynamics of polyanions. Additionally, MD studies reveal that the number of polymer/water hydrogen bonds increases from 5.3 to 6.2, per monomer, as the number of  $K^+$  ions close to the polymer decreases, which also suggests that free water responsible for water electrolysis is reduced with an increase in the concentration of the electrolyte. A 2 V symmetric supercapacitor device was demonstrated, which showed suppressed self-discharge typically found in aqueous-based energy storage devices with carbon or organic electrodes. We believe that this fundamental study provides new insights into ionic transport behavior in WiPSEs and can be used in the design of cost-effective, nonflammable, and highly ionic conductive electrolytes for large-scale supercapacitor applications.

## EXPERIMENTAL SECTION

**Electrolyte Preparation.** The preparation method for electrolytes has been explained in detail in our previous work.<sup>17,18</sup> Briefly, diluted polyacrylic acid (purchased from Merck Sigma-Aldrich,  $M_w$  250 000) solution was neutralized by potassium hydroxide. The obtained solution was dried and mixed with respective water amounts to get different concentrations of WiPSEs. For example, for PAAK 1:1 solution, 1 g of salt was mixed with 1 g of water.

**WiPSE Characterization. Raman Spectroscopy.** Raman spectra were collected at room temperature for the four samples and also for pure water, keeping the samples inside the NMR tubes to avoid drying out of the gels. The collection point was chosen to be 100  $\mu$ m below the lower surface of the tube's wall to minimize the contribution in the spectrum from silica (i.e., from the wall of the NMR tube).

**Pulsed-Field Gradient NMR Spectroscopy.** All NMR measurements were conducted on an AVANCE III HD Bruker NMR spectrometer, operating at 14.1 T, equipped with a diff30 probe with a 5 mm RF-coil probe and capable of producing linear magnetic field gradients in the  $z$ -direction up to 1800 G/cm. Correct calibration of the gradient amplifier was verified by obtaining the self-diffusion coefficient of the HDO trace in a standard sample of pure  $D_2O$ ,<sup>35</sup> and temperature was calibrated using an NMR tube with pure methanol or ethylene glycol prior to the experiments.

All samples were prepared in 5 mm NMR to the same height, and attention was paid to reducing the signal and matching the sample's height to that of the gradient coil (ca. 2 cm). The self-diffusion coefficients of water and of the polymer were determined at six temperatures between 10 and 50 °C (including 25 °C) for sample PAAK 1:2 and at 25 °C for all other samples. For the diffusion measurements within the entire temperature range, a regular stimulated echo (PGSTE) pulse sequence was used, as no possible heat convection effects were found when altering the diffusion time of the experiment at the temperature edges. The absence of convection was also confirmed by the double-stimulated echo (DPGSTE) pulse sequence.<sup>36</sup> As shown in Figure S1, there was no difference between the two experiments of PGSTE and DPGSTE, respectively, at a given elevated temperature.

For the  $^1H$  pulsed-field gradient experiments on the water NMR signal, a 16  $\mu$ s 90° pulse, 1.64 s acquisition time, 10 s recycle delay, 100 ms diffusion delay ( $D$ ), 1 ms gradient pulse duration ( $d$ ), and 100 G/cm maximum gradient strength ( $g$ ) were used. For the  $^1H$  pulsed-field gradient experiments on the polymer NMR signal, the same parameters were used apart from a 2.26 s recycle delay and 1600 G/cm for maximum  $g$ . An NMR spectrum is provided in Figure S11.

The intensities of the assigned NMR signals were plotted on a logarithmic axis against  $k$ , given in eq 1

$$k = (\Delta - \delta/3)(\delta \cdot \gamma \cdot g)^2 \quad (1)$$

where  $g$  is the gyromagnetic ratio of the nucleus studied. All water signal attenuations in this study displayed a strictly monoexponential behavior. The self-diffusion coefficients were calculated from least squares fitting of the attenuation curves with nonlinear dependence using the Levenberg–Marquardt method, using eq 2.

$$I(k) = I_0 \exp(-kD) \quad (2)$$

where  $I(k)$  is the NMR signal intensity at a certain  $k$ ,  $I_0$  is the intensity at zero applied gradient strength, and  $D$  is the self-diffusion coefficient.

All polymer signal attenuations in this study displayed a non-monoexponential behavior rather than a curved profile, which is typical for the distribution of self-diffusion coefficients. Hence, for polymer signals, the self-diffusion coefficients were calculated from least squares fitting using the  $\gamma$  distribution function<sup>37</sup> given in eq 3, which provides the mean self-diffusion coefficient and the standard deviation of the distribution.

$$I(k) = I_0 \left( 1 + \frac{k \cdot \sigma^2}{\langle D \rangle} \right)^{-((D)^2 / \sigma^2)} \quad (3)$$

**Ionic Conductivity Measurement.** The ionic conductivity was measured by impedance spectroscopy using a Novocontrol impedance spectrometer with an electrolyte-filled Teflon cavity with platinum (radius 0.56 mm) as electrodes on both sides without applying any DC bias. The length of the cavity was 0.305 mm. The temperature was varied using an electrical heater and liquid nitrogen within a cryostat, with an error deviation of  $\pm 2$  °C.

**Molecular Dynamics.** Classical molecular dynamics (MD) simulations of PAAK in an aqueous solution were performed in three different PAAK/water concentrations: 1:1, 1:2, 1:4, and 1:6. The simulated systems (illustration in Figure S2) were composed of 43,000 water molecules,  $N$  (140 for 1:1, 70 for 1:2, 35 for 1:4, and 24 for 1:6) PAA<sup>-</sup> polymers (with 50 monomers each), and  $50 \times N$  potassium ions. The initial configurations were prepared by randomly inserting the molecules and ions within a huge cubic box under an atomic minimum distance criterion of 4 Å.<sup>38</sup> The systems were thermalized over 5 ns under a pressure ( $P$ ) of 10 bar and a temperature ( $T$ ) of 298.15 K. Sequentially, a second more extended thermalization (15 ns) was performed under room pressure and temperature conditions ( $P = 1$  bar and  $T = 298.15$  K). The thermalized systems were then simulated for more than 10 ns in the production phase, which was carried out in an NPT ensemble as well ( $P = 1$  bar and  $T = 298.15$  K).

The OPLS-AA<sup>39</sup> and SPC/E<sup>40</sup> force fields were adopted for the polymer and water molecules, respectively, and the force field proposed by Beglov and Roux was adopted for potassium.<sup>41</sup> Such a force field combination was recently recommended in a benchmark study about the thermodiffusion of ions in aqueous solution.<sup>42</sup> The initial geometry of the polymer (see the SI) was obtained by geometry optimization at the DFT/M06/6-31G(d,p) theory level, and its atomic charges were determined by fitting the DFT electrostatic potential using the Merz–Singh–Kollman scheme<sup>43</sup> combined with the polarizable continuum model (PCM) to account for the solvent polarization effects. Both the geometry and the atomic charges of the polymer were calculated in the presence of the counterions, for the sake of the charge neutralization of the system. On average, the atomic charges of the potassium ions were calculated to be 0.9+ at the DFT level, and this charge substituted the original 1+ charge of the model proposed by Beglov and Roux.<sup>41</sup>

The pressure and temperature were controlled by the Berendsen barostat<sup>44</sup> ( $\tau = 2$  ps) and the velocity rescaling thermostat<sup>45</sup> ( $\tau = 0.1$  ps), respectively. All of the short-range intermolecular interactions were computed inside a cutoff radius of 1.4 Å, while the long-range correction for electrostatic interactions was treated with the smooth particle-mesh Ewald method<sup>46</sup> using cubic interpolation and a Fourier spacing of 12 Å. The equations of motion were integrated using the leapfrog algorithm,<sup>47</sup> with a time step of 1 fs, and constraints in all H bonds by using the LINCS algorithm.<sup>48</sup> The center of mass motion was linearly removed for the whole system every 200 fs. The simulations were performed using the Gromacs 2020.4 package.<sup>49</sup>

**Electrode Preparation and Electrochemical Characterization.** To prepare activated carbon (AC), the activated carbon ink was purchased from redox.me (<https://redox.me/products/activated-carbon-ink-100-ml-water-based>) developed by Ligna Energy AB. The purchased ink was used as received without any modification. The slurry was coated on graphite foil (purchased from SGL Carbon, Germany). The coated film was dried in a hot air oven at 60 °C for 2 h. Thereafter, the electrodes were cut for coin cell fabrication. The AC electrode has a mass loading of 10–12 mg/cm<sup>2</sup>. CR2032-type coin cells were prepared at ambient conditions, and grade A glass microfibers were used as a separator. All of the electrochemical characterization was performed using a VSP-3e multichannel potentiostat.  $Q_c/Q_d$  was estimated by performing a galvanostatic charge–discharge (GCD) experiment, where devices were charged and discharged up to the desired potential for five cycles each at a 1 A/g current rate. The last cycle was used to analyze the number of charges for both the charge and discharge steps. Self-discharge was investigated by performing five cycles of GCD and then holding the potential at the cutoff potential for 1 h, followed by open circuit voltage measurement for 5 days.

## ■ ASSOCIATED CONTENT

### SI Supporting Information

The Supporting Information is available free of charge at <https://pubs.acs.org/doi/10.1021/acs.chemmater.3c01089>.

Data of Raman spectra of the polymer electrolyte; ionic conductivity with temperature variation; NMR diffusometry data; K<sup>+</sup> ion coordination with the polymer and water oxygen; mean square displacement; cyclic voltammetry; galvanostatic charge–discharge; and self-discharge plots of the symmetric supercapacitor device (PDF)

## ■ AUTHOR INFORMATION

### Corresponding Authors

Ziyaiddin Khan – *Laboratory of Organic Electronics, Department of Science and Technology, Linköping University, SE-60174 Norrköping, Sweden; [orcid.org/0000-0002-8242-7547](https://orcid.org/0000-0002-8242-7547); Email: [ziyaiddin.khan@liu.se](mailto:ziyaiddin.khan@liu.se)*

Xavier Crispin – *Laboratory of Organic Electronics, Department of Science and Technology, Linköping University, SE-60174 Norrköping, Sweden; [orcid.org/0000-0001-8845-6296](https://orcid.org/0000-0001-8845-6296); Email: [xavier.crispin@liu.se](mailto:xavier.crispin@liu.se)*

### Authors

Anna Martinelli – *Department of Chemistry and Chemical Engineering, Chalmers University of Technology, Gothenburg SE-41296, Sweden; [orcid.org/0000-0001-9885-5901](https://orcid.org/0000-0001-9885-5901)*

Leandro R. Franco – *Department of Engineering and Physics, Karlstad University, 65188 Karlstad, Sweden; [orcid.org/0000-0002-8692-3396](https://orcid.org/0000-0002-8692-3396)*

Divyaratan Kumar – *Laboratory of Organic Electronics, Department of Science and Technology, Linköping University, SE-60174 Norrköping, Sweden*

Alexander Idström – *Department of Chemistry and Chemical Engineering, Chalmers University of Technology, Gothenburg SE-41296, Sweden*

Lars Evenäs – *Department of Chemistry and Chemical Engineering, Chalmers University of Technology, Gothenburg SE-41296, Sweden; [orcid.org/0000-0002-6580-0610](https://orcid.org/0000-0002-6580-0610)*

C. Moyses Araujo – *Department of Engineering and Physics, Karlstad University, 65188 Karlstad, Sweden; Department of Physics and Astronomy, Uppsala University, 75120 Uppsala, Sweden; [orcid.org/0000-0001-5192-0016](https://orcid.org/0000-0001-5192-0016)*

Complete contact information is available at:

<https://pubs.acs.org/doi/10.1021/acs.chemmater.3c01089>

### Author Contributions

Z.K. and X.C. conceived the idea. Z.K. synthesized electrolytes, fabricated electrodes and supercapacitor devices, performed electrochemical characterization, and analyzed the data. A.M., A.I., and L.E. performed Raman and NMR spectroscopic experiments and analyzed the data. L.R.F. and C.M.A. performed all of the simulation studies. D.K. performed temperature-dependent ionic conductivity data and helped in electrode fabrications. X.C. supervised the project. The manuscript was written through contributions of all authors. All authors have given approval to the final version of the manuscript.

### Notes

The authors declare no competing financial interest.

## ■ ACKNOWLEDGMENTS

This work was primarily supported by the Swedish Energy Agency (P52023-1), ÅForsk (22-134, 21-130), and the Knut and Alice Wallenberg Foundation (KAW 2020.0174). This project is also financed through the Swedish Electricity Storage and Balancing Centre (SESBC). The Centre is funded by the Swedish Energy Agency together with 5 academic and 26 non-academic partners. In particular, the authors acknowledge Ligna Energy for their contribution and support to the project. This work also includes some support from the Swedish Government Strategic Research Area in Materials Science on Functional Materials at Linköping University (Faculty Grant SFO-Mat-LiU No. 2009-00971), from the Swedish Research Council (2020-05223) and STandUP for Energy collaboration. The computational infrastructure has been provided by the Swedish National Infrastructure for Computing (SNIC) at the National Supercomputer Centre (NSC) at Linköping University. The NMR measurements were carried out at the Swedish NMR Centre in Gothenburg, Sweden. Z.K. thanks Zia

Ullah Khan for the help in temperature-dependent ionic conductivity measurements.

## REFERENCES

- (1) Sankaralingam, R. K.; Seshadri, S.; Sunarso, J.; Bhatt, A. I.; Kapoor, A. Overview of the factors affecting the performance of vanadium redox flow batteries. *J. Energy Storage* **2021**, *41*, No. 102857.
- (2) Ali, M. H.; Slaifstein, D.; Ibanez, F. M.; Zugschwert, C.; Pugach, M. In *Power Management Strategies for Vanadium Redox Flow Battery and Supercapacitors in Hybrid Energy Storage Systems*, 2022 IEEE PES Innovative Smart Grid Technologies Conference Europe (ISGT-Europe), Oct 10–12, 2022; pp 1–5.
- (3) (a) Xu, K. Electrolytes and Interphases in Li-Ion Batteries and Beyond. *Chem. Rev.* **2014**, *114*, 11503–11618. (b) Li, M.; Hicks, R. P.; Chen, Z.; Luo, C.; Guo, J.; Wang, C.; Xu, Y. Electrolytes in Organic Batteries. *Chem. Rev.* **2023**, *123*, 1712–1773. (c) Kumar, D.; Khan, Z.; Ail, U.; Phopase, J.; Berggren, M.; Gueskine, V.; Crispin, X. Self-Discharge in Batteries Based on Lignin and Water-in-Polymer Salt Electrolyte. *Adv. Energy Sustainability Res.* **2022**, *3*, No. 2200073.
- (4) Fan, X.; Wang, C. High-voltage liquid electrolytes for Li batteries: progress and perspectives. *Chem. Soc. Rev.* **2021**, *50*, 10486–10566.
- (5) Xu, K.; Wang, C. Batteries: Widening voltage windows. *Nat. Energy* **2016**, *1*, No. 16161.
- (6) Suo, L.; Borodin, O.; Gao, T.; Olguin, M.; Ho, J.; Fan, X.; Luo, C.; Wang, C.; Xu, K. “Water-in-salt” electrolyte enables high-voltage aqueous lithium-ion chemistries. *Science* **2015**, *350*, 938–943.
- (7) (a) Liang, T.; Hou, R.; Dou, Q.; Zhang, H.; Yan, X. The Applications of Water-in-Salt Electrolytes in Electrochemical Energy Storage Devices. *Adv. Funct. Mater.* **2021**, *31*, No. 2006749. (b) Shen, Y.; Liu, B.; Liu, X.; Liu, J.; Ding, J.; Zhong, C.; Hu, W. Water-in-salt electrolyte for safe and high-energy aqueous battery. *Energy Storage Mater.* **2021**, *34*, 461–474. (c) Khan, Z.; Kumar, D.; Crispin, X. Does Water-in-salt Electrolyte Subdue Issues of Zn Batteries? *Adv. Mater.* **2023**, No. 2300369.
- (8) Xiao, D.; Zhang, L.; Li, Z.; Dou, H.; Zhang, X. Design strategies and research progress for Water-in-Salt electrolytes. *Energy Storage Mater.* **2022**, *44*, 10–28.
- (9) Lv, T.; Suo, L. Water-in-salt widens the electrochemical stability window: Thermodynamic and kinetic factors. *Curr. Opin. Electrochem.* **2021**, *29*, No. 100818.
- (10) Yokoyama, Y.; Fukutsuka, T.; Miyazaki, K.; Abe, T. Origin of the Electrochemical Stability of Aqueous Concentrated Electrolyte Solutions. *J. Electrochem. Soc.* **2018**, *165*, A3299.
- (11) Borodin, O.; Suo, L.; Gobet, M.; Ren, X.; Wang, F.; Faraone, A.; Peng, J.; Olguin, M.; Schroeder, M.; Ding, M. S.; et al. Liquid Structure with Nano-Heterogeneity Promotes Cationic Transport in Concentrated Electrolytes. *ACS Nano* **2017**, *11*, 10462–10471.
- (12) Li, Z.; Bouchal, R.; Mendez-Morales, T.; Rollet, A. L.; Rizzi, C.; Le Vot, S.; Favier, F.; Rotenberg, B.; Borodin, O.; Fontaine, O.; Salanne, M. Transport Properties of Li-TFSI Water-in-Salt Electrolytes. *J. Phys. Chem. B* **2019**, *123*, 10514–10521.
- (13) McEldrew, M.; Goodwin, Z. A. H.; Bi, S.; Bazant, M. Z.; Kornyshev, A. A. Theory of ion aggregation and gelation in superconcentrated electrolytes. *J. Chem. Phys.* **2020**, *152*, No. 234506.
- (14) (a) Ko, S.; Yamada, Y.; Yamada, A. A 62 m K-ion aqueous electrolyte. *Electrochem. Commun.* **2020**, *116*, No. 106764. (b) Martin, P.-A.; Árén, F.; Johansson, P. (Localized) Highly Concentrated Electrolytes for Calcium Batteries. *Batteries Supercaps* **2023**, *6*, No. e202300003.
- (15) Khan, Z.; Ail, U.; Ajjan, F. N.; Phopase, J.; Kim, N.; Kumar, D.; Khan, Z. U.; Nilsson, J.; Inganäs, O.; Berggren, M.; Crispin, X. Towards printable water-in-polymer salt electrolytes for high power organic batteries. *J. Power Sources* **2022**, *524*, No. 231103.
- (16) He, X.; Yan, B.; Zhang, X.; Liu, Z.; Bresser, D.; Wang, J.; Wang, R.; Cao, X.; Su, Y.; Jia, H.; et al. Fluorine-free water-in-ionomer electrolytes for sustainable lithium-ion batteries. *Nat. Commun.* **2018**, *9*, No. 5320.
- (17) Khan, Z.; Ail, U.; Nadia Ajjan, F.; Phopase, J.; Ullah Khan, Z.; Kim, N.; Nilsson, J.; Inganäs, O.; Berggren, M.; Crispin, X. Water-in-Polymer Salt Electrolyte for Slow Self-Discharge in Organic Batteries. *Adv. Energy Sustainability Res.* **2022**, *3*, No. 2100165.
- (18) Kumar, D.; Ail, U.; Wu, Z.; Björk, E. M.; Berggren, M.; Gueskine, V.; Crispin, X.; Khan, Z. Zinc salt in “Water-in-Polymer Salt Electrolyte” for Zinc-Lignin Batteries: Electroactivity of the Lignin Cathode. *Adv. Sustainable Syst.* **2023**, *7*, No. 2200433.
- (19) Wilske, B.; Bai, M.; Lindenstruth, B.; Bach, M.; Rezaie, Z.; Frede, H.-G.; Breuer, L. Biodegradability of a polyacrylate superabsorbent in agricultural soil. *Environ. Sci. Pollut. Res.* **2014**, *21*, 9453–9460.
- (20) Angell, C. A.; Imrie, C. T.; Ingram, M. D. From simple electrolyte solutions through polymer electrolytes to superionic rubbers: some fundamental considerations. *Polym. Int.* **1998**, *47*, 9–15.
- (21) Wang, J. H. Effect of Ions on the Self-diffusion and Structure of Water in Aqueous Electrolytic Solutions. *J. Phys. Chem. A* **1954**, *58*, 686–692.
- (22) Tsukida, N.; Muranaka, H.; Ide, M.; Maeda, Y.; Kitano, H. Effect of Neutralization of Poly(acrylic acid) on the Structure of Water Examined by Raman Spectroscopy. *J. Phys. Chem. B* **1997**, *101*, 6676–6679.
- (23) Kaminsky, M. Ion-solvent interaction and the viscosity of strong-electrolyte solutions. *Discuss. Faraday Soc.* **1957**, *24*, 171–179.
- (24) (a) Nomura, H.; Yoshiaki, T.; Ernest, V. R.; Yutaka, M. Raman Study of Aqueous Solutions of Tetraalkylammonium and Bis-(tetraalkylammonio) Electrolytes. *Bull. Chem. Soc. Jpn.* **1980**, *53*, 1825–1831. (b) Rull, F.; de Saja, J. A. Effect of electrolyte concentration on the Raman spectra of water in aqueous solutions. *J. Raman Spectrosc.* **1986**, *17*, 167–172.
- (25) Terpstra, P.; Combes, D.; Zwick, A. Effect of salts on dynamics of water: A Raman spectroscopy study. *J. Chem. Phys.* **1990**, *92*, 65–70.
- (26) Burikov, S. A.; Dolenko, T. A.; Velikotnyi, P. A.; Sugonyaev, A. V.; Fadeev, V. V. The effect of hydration of ions of inorganic salts on the shape of the Raman stretching band of water. *Opt. Spectrosc.* **2005**, *98*, 235–239.
- (27) Koda, S.; Nomura, H.; Nagasawa, M. Raman spectroscopic studies on the interaction between counterion and polyion. *Biophys. Chem.* **1982**, *15*, 65–72.
- (28) Röding, M.; Bernin, D.; Jonasson, J.; Särkkä, A.; Topgaard, D.; Rudemo, M.; Nydén, M. The gamma distribution model for pulsed-field gradient NMR studies of molecular-weight distributions of polymers. *J. Magn. Reson.* **2012**, *222*, 105–111.
- (29) Tanaka, K. Measurements of self-diffusion coefficients of water in pure water and in aqueous electrolyte solutions. *J. Chem. Soc., Faraday Trans. 1* **1975**, *71*, 1127–1131.
- (30) Allen, M. P.; Tildesley, D. J. *Computer Simulation of Liquids*; Oxford University Press, 2017.
- (31) Agar, J. N.; Mou, C. Y.; Lin, J. L. Single-ion heat of transport in electrolyte solutions: a hydrodynamic theory. *J. Phys. Chem. A* **1989**, *93*, 2079–2082.
- (32) Holz, M.; Heil, S. R.; Sacco, A. Temperature-dependent self-diffusion coefficients of water and six selected molecular liquids for calibration in accurate 1H NMR PFG measurements. *Phys. Chem. Chem. Phys.* **2000**, *2*, 4740–4742.
- (33) (a) McConville, P.; Pope, J. M. A comparison of water binding and mobility in contact lens hydrogels from NMR measurements of the water self-diffusion coefficient. *Polymer* **2000**, *41*, 9081–9088. (b) He, X.; Fowler, A.; Toner, M. Water activity and mobility in solutions of glycerol and small molecular weight sugars: Implication for cryo- and lyopreservation. *J. Appl. Phys.* **2006**, *100*, No. 074702. (c) Caccavo, D.; Cascone, S.; Lamberti, G.; Barba, A. A. Hydrogels: experimental characterization and mathematical modelling of their mechanical and diffusive behaviour. *Chem. Soc. Rev.* **2018**, *47*, 2357–2373.

(34) Przulski, J.; Siekierski, M.; Wieczorek, W. Effective medium theory in studies of conductivity of composite polymeric electrolytes. *Electrochim. Acta* **1995**, *40*, 2101–2108.

(35) Holz, M.; Weingartner, H. Calibration in accurate spin-echo self-diffusion measurements using  $^1\text{H}$  and less-common nuclei. *J. Magn. Reson.* **1991**, *92*, 115–125.

(36) Jerschow, A.; Müller, N. Suppression of Convection Artifacts in Stimulated-Echo Diffusion Experiments. Double-Stimulated-Echo Experiments. *J. Magn. Res.* **1997**, *125*, 372–375.

(37) Röding, M.; Bernin, D.; Jonasson, J.; Särkkä, A.; Topgaard, D.; Rudemo, M.; Nydén, M. The gamma distribution model for pulsed-field gradient NMR studies of molecular-weight distributions of polymers. *J. Magn. Res.* **2012**, *222*, 105–111.

(38) Martínez, L.; Andrade, R.; Birgin, E. G.; Martínez, J. M. PACKMOL: A package for building initial configurations for molecular dynamics simulations. *J. Comput. Chem.* **2009**, *30*, 2157–2164.

(39) Jorgensen, W. L.; Maxwell, D. S.; Tirado-Rives, J. Development and Testing of the OPLS All-Atom Force Field on Conformational Energetics and Properties of Organic Liquids. *J. Am. Chem. Soc.* **1996**, *118*, 11225–11236.

(40) Berendsen, H. J. C.; Grigera, J. R.; Straatsma, T. P. The missing term in effective pair potentials. *J. Phys. Chem. A* **1987**, *91*, 6269–6271.

(41) Beglov, D.; Roux, B. Finite representation of an infinite bulk system: Solvent boundary potential for computer simulations. *J. Chem. Phys.* **1994**, *100*, 9050–9063.

(42) Rezende Franco, L.; Sehnem, A. L.; Figueiredo Neto, A. M.; Coutinho, K. Molecular Dynamics Approach to Calculate the Thermodiffusion (Soret and Seebeck) Coefficients of Salts in Aqueous Solutions. *J. Chem. Theory Comput.* **2021**, *17*, 3539–3553.

(43) Singh, U. C.; Kollman, P. A. An approach to computing electrostatic charges for molecules. *J. Comput. Chem.* **1984**, *5*, 129–145.

(44) Berendsen, H. J. C.; Postma, J. P. M.; Gunsteren, W. F. V.; DiNola, A.; Haak, J. R. Molecular dynamics with coupling to an external bath. *J. Chem. Phys.* **1984**, *81*, 3684–3690.

(45) Bussi, G.; Donadio, D.; Parrinello, M. Canonical sampling through velocity rescaling. *J. Chem. Phys.* **2007**, *126*, No. 014101.

(46) Essmann, U.; Perera, L.; Berkowitz, M. L.; Darden, T.; Lee, H.; Pedersen, L. G. A smooth particle mesh Ewald method. *J. Chem. Phys.* **1995**, *103*, 8577–8593.

(47) Hockney, R. W.; Goel, S. P.; Eastwood, J. W. Quiet high-resolution computer models of a plasma. *J. Comput. Phys.* **1974**, *14*, 148–158.

(48) Hess, B.; Bekker, H.; Berendsen, H. J. C.; Fraaije, J. G. E. M. LINCS: A linear constraint solver for molecular simulations. *J. Comput. Chem.* **1997**, *18*, 1463–1472.

(49) Van Der Spoel, D.; Lindahl, E.; Hess, B.; Groenhof, G.; Mark, A. E.; Berendsen, H. J. C. GROMACS: Fast, flexible, and free. *J. Comput. Chem.* **2005**, *26*, 1701–1718.

## Recommended by ACS

### Building Sodium Metal Battery with Polyisoprene-Based Air-Stable Single-Ion Gel Polymer Electrolyte

Sayan Das, Venimadhav Adyam, *et al.*

MAY 10, 2023  
ACS APPLIED ENERGY MATERIALS

READ 

### Formulation and Characterization of PS-Poly(ionic liquid) Triblock Electrolytes for Sodium Batteries

Sneha Malunavar, Maria Forsyth, *et al.*

NOVEMBER 21, 2022  
ACS APPLIED POLYMER MATERIALS

READ 

### The Importance of Morphology on Ion Transport in Single-Ion, Comb-Branched Copolymer Electrolytes: Experiments and Simulations

Sanket Kadulkar, Venkat Ganesan, *et al.*

MARCH 30, 2023  
MACROMOLECULES

READ 

### Polymers with Cyanoethyl Ether and Propanesulfonate Ether Side Chains for Solid-State Li-Ion Battery Applications

Badril Azhar, Chorong-Shyan Chern, *et al.*

MARCH 07, 2023  
ACS APPLIED ENERGY MATERIALS

READ 

Get More Suggestions >